Elastic and inelastic scattering of ^{16}O and ^{18}O on ^{28}Si at 56 MeV incident energy

M. C. Mermaz, M. A. G. Fernandes, A. Greiner, B. T. Kim, and N. Lisbona
DPh-N/BE, CEN Saclay, BP 2, 91190 Gif-sur-Yvette, France
(Received 31 August 1978)

Elastic and inelastic scatterings of ^{16}O and ^{18}O projectiles have been studied on ^{28}Si nucleus at 56 MeV incident energy. Optical model and coupled-channel analyses have been performed in order to define the nature of the optical potential. It has turned out that the enhanced backward angle oscillations that appeared in the angular distribution for the ^{16}O scattering are mainly due to refractive phenomena namely orbiting rather than diffractive phenomena. The potential necessary to reproduce the experimental data has to be surface transparent for ^{16}O projectile, with a pocket in the effective potential in the grazing wave region and with a sharp diffusivity in the imaginary part in order to produce a mirror effect due to strong and abrupt volume absorption. On the other hand the potential necessary to fit the ^{18}O scattering angular distributions is just a normal strong absorptive potential. The absence of any surface transparency in the case of ^{18}O scattering can be attributed to the fact that many direct reaction channels are well Q matched.

[NUCLEAR REACTIONS $^{28}Si(^{16}O, ^{16}O)$ and $^{28}Si(^{18}O, ^{18}O)$, $E_{^{16}O}$, $E_{^{18}O}$ = 56 MeV; elastic and inelastic angular distributions measured between 5° and 71° (lab). Optical model and coupled-channel analysis.]

I. INTRODUCTION

Several elastic scattering experiments of ^{16}O on ^{28}Si have been performed at various incident energies. The general behavior of the elastic cross sections versus the incident energy was investigated and a universal energy-independent potential, called E-18, was proposed.[1] It has turned out in this first series of analyses that neither orbiting nor nuclear rainbow is necessary to account for the experimental data and that strong absorption is only present. Nevertheless a more recent experiment performed at very backward angles up to 180° has shown[2] that orbiting is evident at low energy in the vicinity of the Coulomb barrier. The nuclear rainbow phenomena, already encountered in α-scattering experiment, have also been observed[3] in ^{6}Li elastic scattering on ^{28}Si at high incident energy of 135 MeV.

All these refractive phenomena compete with diffraction: Fresnel diffraction at low incident energy in the vicinity of the Coulomb barrier, and Fraunhoffer at high energy. However, the refractive phenomena, orbiting or nuclear rainbow, can only be seen if the absorption is weak in the region where these processes occur, namely, at the surface. Otherwise diffraction due to the strong absorption dominates.

It is suggested that the backward angle oscillatory rise revealed both in the elastic and in the first 2^+ inelastic angular distributions is the signature of the orbiting phenomena. Such an orbiting should be interpreted by an optical potential. It will be shown that these structured angular distributions will allow us to understand better the nature of the optical model potential.

We have measured angular distributions of the elastic and inelastic scattering of ^{16}O and ^{18}O ions on ^{28}Si, up to the 6.88 MeV 3^- state in ^{28}Si. The experiments were performed at 56 MeV incident ion energy. The data were analyzed in terms of optical model and coupled-channel methods, by using the automatic search computer programs respectively MAGALI and ECIS-73 of J. Raynal.[4] Section III contains optical model analyses of the 56 MeV elastic scattering data and a reanalysis of 55 MeV data of Braun-Munzinger *et al.*[2] In Sec. IV are presented the results of the coupled-channel analysis of the inelastic scattering. A comparison between ^{16}O and ^{18}O scatterings on ^{28}Si is also made.

II. EXPERIMENTAL PROCEDURE

The experiments have been performed using the 56 MeV ^{16}O and ^{18}O ion beams of the FN Tandem Van de Graaff of Saclay. The angular distributions have been measured using a quadrupole-dipole-dipole-dipole (QDDD) magnetic spectrometer. A two stage gas proportional counter was used in order to measure the position and to identify the heavy fragments. The total length of the counter was 50 cm. The 99% enriched ^{28}Si target on a carbon backing had a thickness of 128 $\mu g/cm^2$. The kinematic corrections made by a quadrupole system allowed a resolution of 120 keV [full width at half maximum (FWHM)]. The horizontal aper-

ture of the spectrometer in the reaction plane was 1° and the vertical aperture 2°. The angular distributions have been measured between 5° and 71° in the laboratory system in steps of 1.5° at forward angles and 1° at backward angles.

The cross sections were evaluated using a formula given by Marion and Young[5] for the charge state distribution. It was verified that these values agree well with the experimental ones.[5] The absolute values of the inelastic cross sections were obtained by normalizing the very forward angle elastic scattering data to Rutherford predictions. A typical spectrum of ^{16}O scattered by a ^{28}Si target is displayed in Fig. 1. The ^{12}C and ^{16}O contaminants unfortunately did not allow the study of the 6.28 MeV 3^+ unnatural parity state, which may be populated only by a two-step process.

III. OPTICAL MODEL ANALYSIS

Recently an optical model analysis of ^{16}O scattering on ^{28}Si measured between 45 and 63 MeV incident energy had been performed, and showed[6] that the optical potential has to be surface transparent, i.e., $V/W \gg 1$, $r_V > r_W$, and $a_V > a_W$ in order to see the orbiting phenomena. Furthermore it should be noticed that the diffusivity of the imaginary well is close to the wave length of the projectile, which produces a backward angle rise of the angular distribution with an oscillatory behavior. This can be interpreted as a mirror effect due to an abrupt strong absorption.

In this section we study how surface transparency relates to the experimental oscillations appearing in an angular region between 60° and 100° c.m. Secondly we discuss the physical meaning of the sharp diffusivity by reanalyzing the very backward angle data of Braun-Munzinger *et al.*,[2] and finally we examine the characteristics of the optical potentials derived from the ones published in the literature. Throughout this optical model analysis we have used the elastic scattering automatic search code MAGALI.[4]

In order to study the role of the surface transparency we have considered three different kinds of optical potential, by changing the ratio between V and W and the absolute value of V, as listed in Table I. The equal geometries for the real and imaginary parts were chosen in order to have as few parameters as possible. In Fig. 2 are presented the results of the optical model analysis of the 56 MeV ^{16}O scattering data for these three potentials. The transmission coefficients obtained using these three potentials are also inset in the figure.

As can be seen in Fig. 2, the potential S-1 (solid curve) gives the best fit not only for the experimental slope of the Fresnel diffraction but also for the behavior of the observed oscillations. The optical model penetrability shows that this potential is transparent only at surface and thus volume absorption is present. The total reaction

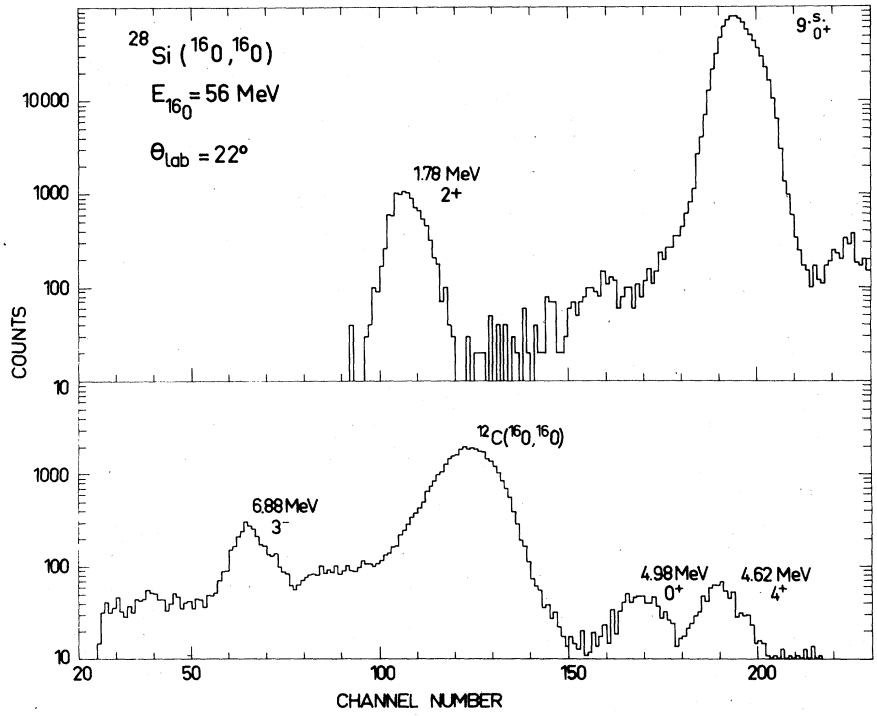

FIG. 1. Typical position spectrum of the elastic and inelastic scattering of 56 MeV ^{16}O from ^{28}Si at $\theta_{lab} = 22°$.

TABLE I. Optical model parameters for the elastic scattering ($r_c = r_v$). The parameters correspond to the ^{16}O elastic scattering on ^{28}Si measured at 56 and 55 MeV incident energy. The automatic search code MAGALI has been used; see text.

Family	V (MeV)	r_v (fm)	a_v (fm)	W (MeV)	r_w (fm)	a_w (fm)	σ_R (mb)	χ^2/N	Energy (MeV)
S-1	50.00	1.261	0.545	6.22	1.261	0.545	1294	27	56.0
S-2	10.00	1.383	0.509	0.60	1.383	0.509	651	33	56.0
S-3	50.00	1.261	0.545	25.00	1.261	0.545	1405	622	56.0
S-20	48.83	1.266	0.527	7.34	1.222	0.209	1219	52	55.0
S-21	48.83	1.263	0.532	7.93	1.197	0.450	1227	76	55.0
S-22	10.00	1.387	0.423	4.21	1.359	0.239	1032	53	55.0
A-2	24.08	1.310	0.557	5.25	1.321	0.675	1374	34	56.0
E-18-2	11.41	1.359	0.588	23.38	1.230	0.532	1269	...	56.0

cross section is equal to 1294 mb. A depth of 6.2 MeV for the imaginary part compared to a depth of 50.0 MeV for the real part is enough to suppress any interior contributions to the elastic scattering. Such a potential exhibiting a surface transparency has been proposed in order to reproduce direct transfer angular distributions at forward angles[7] as well as elastic and inelastic scattering data.[8]

The potential S-2 also produces a good fit but is very shallow and has a very weak absorption in the interior region. Indeed the total reaction cross section is far too small and an unrealistic value of $\sigma_R = 651$ mb. The transmission coefficients show a large volume transparency. The angular distribution presents oscillations, but not any backward angle rise. The slope of the differential cross section is exponentially decreasing.

The potential S-3 is just a strong absorptive potential (see the inset of Fig. 2) and can not explain the oscillatory angular distribution at backward angles. This potential gives rise only to a pure Fresnel diffractive scattering picture.

We have also plotted the effective potentials,

$$V_{\text{eff}}(r) = V_N(r) + V_c(r) + \frac{l(l+1)\hbar^2}{2\mu r^2},$$

for S-1 and S-2 in Fig. 3. The potential S-1 ex-

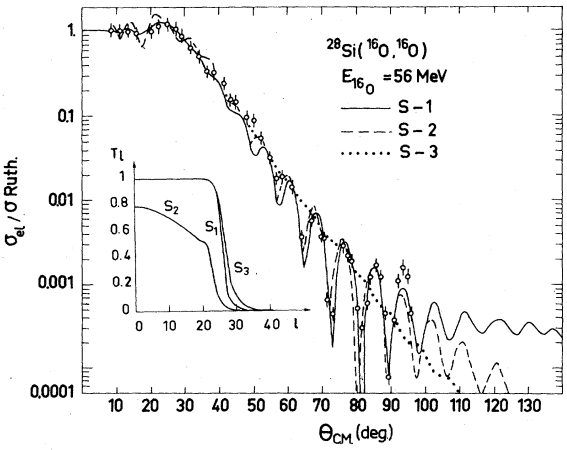

FIG. 2. Optical model fits obtained with the potentials S-1, S-2, and S-3 of the ^{16}O elastic scattering angular distributions of ^{28}Si. The penetrabilities versus partial waves are inset for each potential.

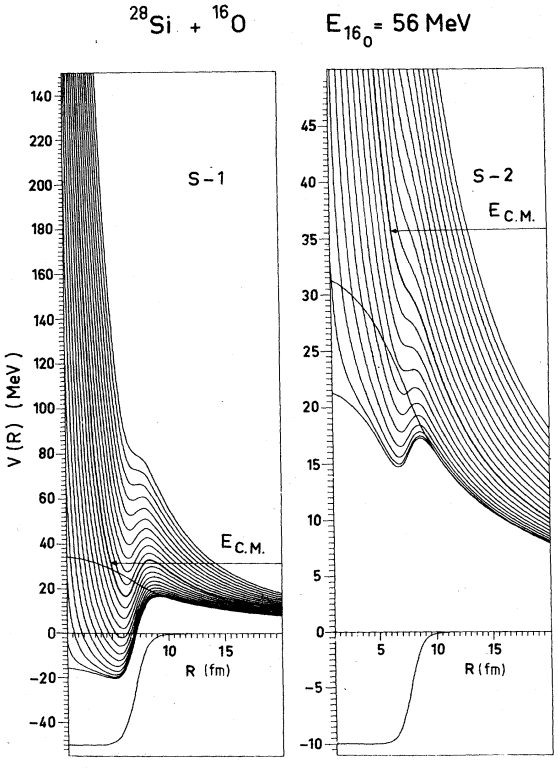

FIG. 3. Effective potentials for the potentials S-1 and S-2. The thick solid lines represent effective potentials at the grazing partial wave. The real part of nuclear potentials as well as the Coulomb part are also drawn.

hibits a pocket for several partial waves near the grazing wave ($T_{l_g} = 0.5$) at $l_g = 26$, while the S-2 family presents no pocket near its grazing wave $l_g = 22$. The existence of a pocket near the grazing wave and a weak absorption near the potential barrier for S-1 implies that this potential satisfies the conditions for orbiting, which is responsible for the wiggles in the 60°–100° angular region. The exponentially decreasing oscillatory patterns for S-2 are not due to orbiting but due mainly to contribution from the volume transparent interior region.

It is noted that orbiting depends upon the shape and the depth of the real potential and, in principle, should give us some information about the real potential. Miller[9] has obtained the maximum energy equal to

$$E_{\text{orb}} = \max_r [V(r) + \tfrac{1}{2} r V'(r)] ,$$

at which classical orbiting disappears, from the requirements that $V'_{\text{eff}}(r) = V''_{\text{eff}}(r) = 0$, where the prime implies the derivative with respect to the radial distance. In Fig. 4 we display the limits of the real potential parameters for orbiting at $E_{\text{c.m.}} = 35.63$ MeV, which is our incident c.m. energy. Orbiting can not occur in the region below the solid line in the figure. As can be seen, we should not expect an orbiting phenomenon in the S-2 potential. Hence the orbiting allows us to determine the limits of the real part of the optical potential.

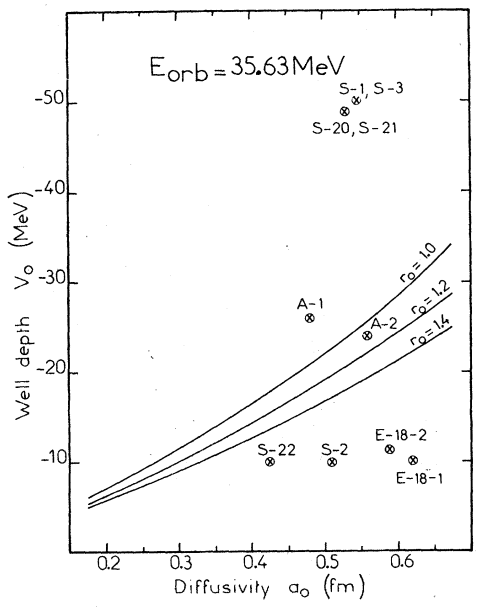

FIG. 4. Real Woods-Saxon potential parameter limits for orbiting at $E_{\text{orb}} = 35.63$ MeV. This energy corresponds to the ^{16}O bombarding energy of 56 MeV in the lab system.

We conclude that the surface transparent potential with a depth deep enough can reproduce the experimental data up to 100° (c.m.) in the angular distribution. The shallow potential with a large value of V/W gives a good fit in this particular angular region but an unrealistic total reaction cross section as mentioned earlier. The strong absorption potential produces only a diffractive pattern provided the Coulomb barrier is correctly located. It has turned out that the strong absorption potential and/or the shallow potential are not adequate to describe the ^{16}O+^{28}Si scattering.

The 55 MeV elastic angular distribution measured up to 180° provides additional information about the nature of the optical potential. Attempts to obtain a good fit with an equal geometry potential as in the previous case had failed completely for this structured angular distributions. We thus use a six-parameter potential. The potential, listed as S-20 in Table I, with a large surface transparency furnishes an excellent fit to this elastic experimental data, as it is displayed in Fig. 5. The real part of this potential is very similar to S-1 and thus guarantees orbiting (see Fig. 4). Another characteristic of this potential is a small diffusivity of the imaginary part. We have attempted to find a potential of which a_W is close to a_V. The potential found, S-21, is also tabulated in Table I. The results of this calculation are displayed in Fig. 5 and compared with that obtained with S-20. We obtain a fit as good as that of S-20 up to 100° angular region, but with smaller cross sections than an experimental one at very backward angles. The transmission coefficients for S-20 and S-21 show a normal volume absorption and the reaction cross sections are respectively, 1219 and 1227 mb. It is thus found that a small value of the diffusivity of the imaginary part enhances the oscillations at backward angles. This enhancement can be explained as a reflection due to an abrupt volume absorption (mirror effect). As soon as the diffusivity of the imaginary part is at least twice the wavelength of the projectile ($\lambda\!\!\!^{-} = 0.24$ fm), the oscillations at backward angles are due only to orbiting.

We further study the mirror effect on this backward angle scattering, by reducing the well depth of the real part to 10 MeV so that the effective potential exhibits no pocket in the grazing wave region, but by keeping still a very small imaginary diffusivity. As shown in Fig. 6, such potential S-22 can not reproduce the very backward angle cross sections either. It also shows perfectly normal transmission coefficients without any volume transparency: The total reaction cross

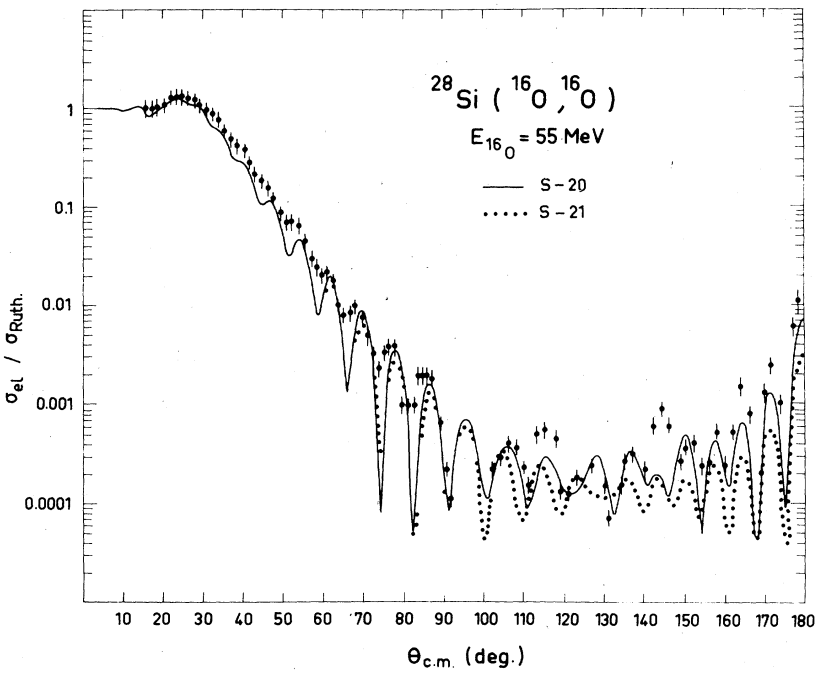

FIG. 5. Optical model fits to the 55 MeV ^{16}O elastic scattering on ^{28}Si with the potentials *S*-20 and *S*-21. The data were taken from Ref. 2.

section is 1032 mb. The calculated shape of the angular distribution is just diffractive and presents also a mirror effect at backward angles. The experimental data thus make it possible to distinguish among the orbiting phenomena, the mirror effect and diffraction due to strong absorption. Only effective potentials with pockets in the grazing wave region and a sharp diffusivity for the imaginary part are able to reproduce correctly the experimental shape at very backward angles.

One may argue whether or not the nature of the optical potential discussed here is still valid to reproduce the general trend of excitation functions. Very recently it has been shown[10] that the general trend of the excitation function as a function of bombarding energy and target atomic number can be reproduced by increasing strongly the

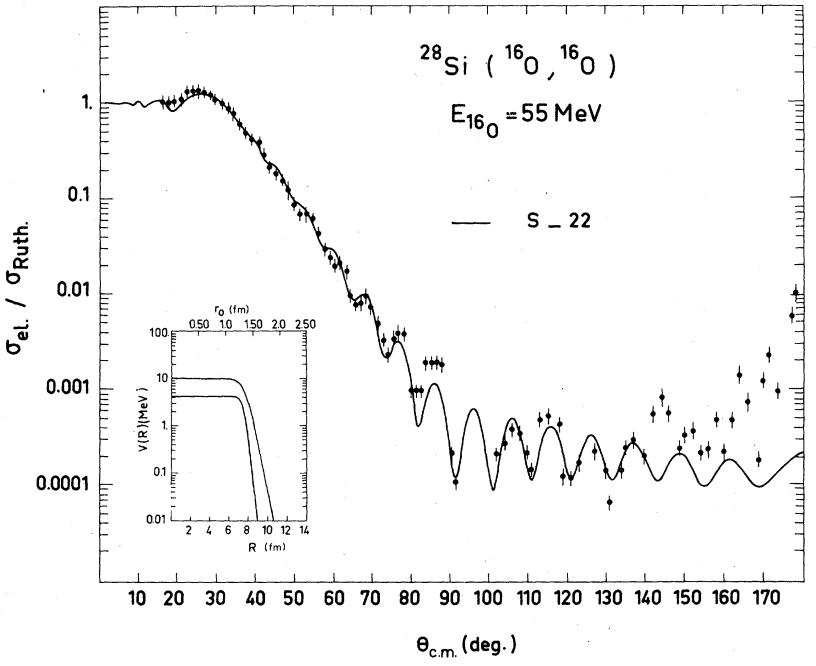

FIG. 6. Same as Fig. 5, but with the potential *S*-22. The real and imaginary potentials in the inset are also drawn in semilogarithmic scale.

absorption (radius of imaginary potential) with increasing bombarding energy and target atomic number, but still keeping the surface transparency and the small diffusivity of the imaginary potential.

Our 56-MeV experimental data have also been fitted with potentials derived from the ones published in the literature. The potential A-2 is from the analysis of 55 MeV data[2] by Udagawa[11] and the potential E-18-2 belongs to the E-18 family of Cramer *et al.*[1] The potential A-2 is a surface transparent one with a pocket for the effective potential in the grazing wave region, while E-18-2 is a strong absorptive potential without any pocket (see also Fig. 4). As can be seen in Fig. 7, the A-2 potential gives an excellent fit, while E-18-2 produces only a diffractive Fresnel type pattern.

In Fig. 8 are displayed the deflection functions of potentials A-2 and E-18-2:

$$\theta_l = 2\frac{\partial \eta_l}{\partial l},$$

where $\eta_l = \delta_l + \sigma_l$, δ_l being the nuclear phase shift and σ_l the pure Coulomb phase shift. The E-18-2 potential exhibits a repulsive behavior for small l values due to strong absorption, while A-2 clearly demonstrates orbiting which is responsible for the oscillatory behavior of the angular distributions at the backward angles.

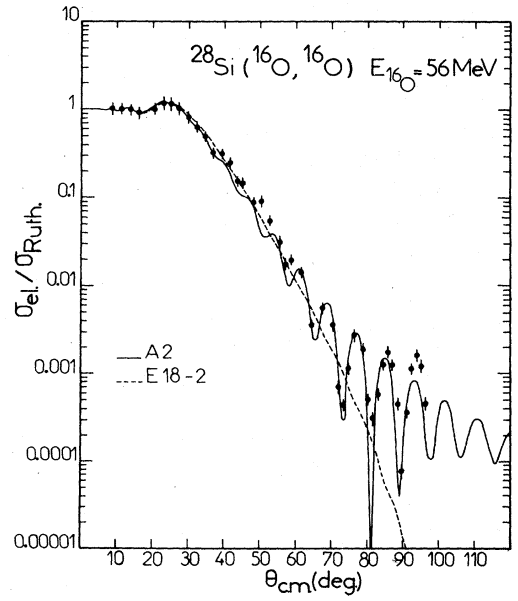

FIG. 7. Same as Fig. 2, but with the potentials A-2 and E-18-2.

IV. COUPLED-CHANNEL ANALYSIS

We have so far discussed the general characteristics of the optical potential which can account for the $^{28}Si + ^{16}O$ elastic scattering. However, it has been speculated[11] that the coupling effect may be important because of the known strong collectivity of ^{28}Si and thus a simple potential description may not be valid for this particular scattering process. Indeed ^{28}Si is known[12] to be a strongly deformed rotational nucleus with an absolute deformation parameter of $|\beta_2| = 0.41$ for a reduced electromagnetic radius of $r_c = 1.20$ fm. Furthermore it is known from intrinsic quadrupole measurements[13,14] and inelastic scattering of polarized protons[15] that this nucleus has an oblate deformation ($\beta_2 < 0$). In this section we have thus investigated the coupled-channel effects on the elastic and inelastic scattering. From this coupled-channel analysis we have also attempted to study the shape and collective property of the ^{28}Si nucleus. Finally we present a comparison between ^{16}O and ^{18}O scattering on ^{28}Si. The coupled-channel automatic search code ECIS-73 (Ref. 4) of Raynal was used for all calculations.

The coupled-channel distorted waves were generated by deforming the standard Woods-Saxon potential, following a paper given by Tamura.[16] The ^{28}Si was assumed to be an axially symmetric deformed rotational nucleus with a surface described as

$$R = R_0[1 + \beta_2 Y_{20}(\theta')],$$

where θ' refers to the body fixed system. The

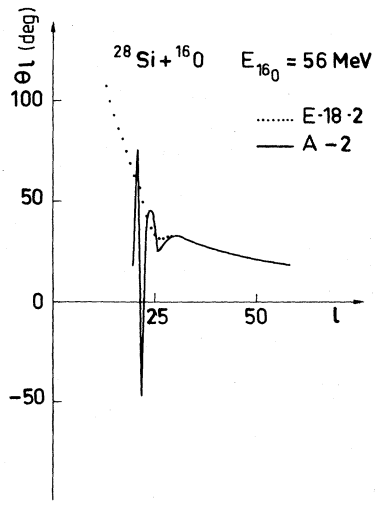

FIG. 8. Deflection functions obtained from the optical model analysis with the potentials A-2 and E-18-2.

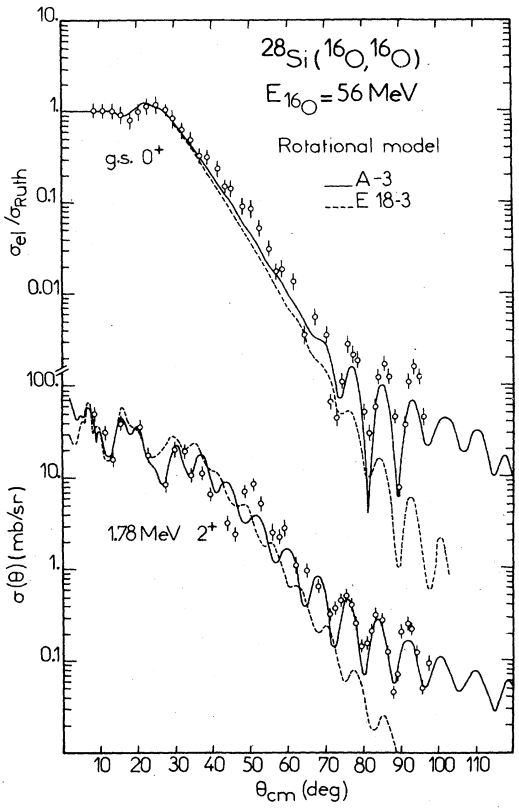

FIG. 9. Coupled-channel analysis for the elastic and 2_1^+ inelastic scattering of 56 MeV ^{16}O from ^{28}Si with the potentials A-3 and E-18-3. The rotational coupling between the 0_g^+ and 2_1^+ states is considered.

coupling potential is derived by expanding the deformed optical potential in terms of Legendre polynomials. The value of the quadrupole deformation parameter β_2 was also searched in this analysis. We shall discuss it later in detail. The higher order multipole deformations were not considered in this work.

Two optical potential families were used as starting points: E-18-1 (Cramer *et al.*[1]) and A-1 (Udagawa[11]). We first consider only a rotational coupling between the 0^+ ground (0_g^+) and the first 2^+ (2_1^+) excited state. The results of calculations are displayed in Fig. 9. The potentials obtained, listed as E-18-3 and A-3 in Table II, are very similar to those from the optical model analysis, E-18-2 and A-2, respectively but less absorptive. The family A-3 exhibiting a weak absorption at the nuclear surface and pockets in the effective potentials near the grazing wave reproduces correctly the elastic as well as inelastic scattering data. The strong absorptive potential E-18-3 gives a good fit only at forward angles, but at backward angles produces very small cross sections both for the elastic and for the inelastic scattering and out-of-phase oscillations for the inelastic scattering case. It is worth noting that the experimental oscillations of the elastic and inelastic cross sections are in phase at backward angles in contradiction to the Blair phase rule for the point object scattering. The fact that E-18-3 exhibits out-of-phase oscillations with data implies that the experimental oscillations are not again due to diffraction phenomena but due to orbiting resonance.

In Fig. 10 are presented the results of the study of the coupling effects from the higher excited states, considering the $0_g^+ - 2_1^+ - 4_1^+$, ground state rotational band coupling. The potential obtained, A-9, has the same real part as A-3, but a more transparent imaginary potential (see Table II). It is thus concluded that the transparency has to be increased as more states are coupled explicitly. In order to illustrate the striking difference between strong absorptive potential and surface transparent potential we have plotted, respectively the potentials E-18-3 and A-9 in Figs. 11 and 12.

It is very interesting to examine the $0_g^+ - 2_1^+$ transition matrix elements produced by these

TABLE II. Optical model parameters for coupled-channel analysis ($r_c = r_v$). The parameters correspond to ^{16}O elastic and inelastic scattering on ^{28}Si measured at 56 and 55 MeV incident energy. The coupled-channel automatic search code ECIS-73 has been used; see text.

Family	V (MeV)	r_v (fm)	a_v (fm)	W (MeV)	γ_W (fm)	a_W (fm)	σ_R (mb)	χ^2/N	Energy (MeV)
A-1	26.08	1.359	0.480	4.91	1.303	0.252	1352	···	56.0
A-3	26.92	1.355	0.500	4.53	1.280	0.590	1383	54	56.0
A-9	26.92	1.355	0.500	4.53	1.242	0.400	1339	···	56.0
A-10	27.26	1.391	0.460	5.09	1.253	0.418	1387	···	56.0
E-18-1	10.00	1.350	0.618	23.40	1.230	0.552	1278	···	56.0
E-18-3	19.13	1.384	0.547	22.92	1.252	0.598	1487	121	56.0
S-5	50.00	1.245	0.539	5.25	1.245	0.539	1268	63	56.0
S-6	50.00	1.245	0.539	4.75	1.245	0.539	1278	69	56.0
S-23	48.01	1.252	0.525	4.94	1.233	0.231	1244	73	55.0
S-24	48.48	1.254	0.519	6.74	1.244	0.201	1312	105	55.0

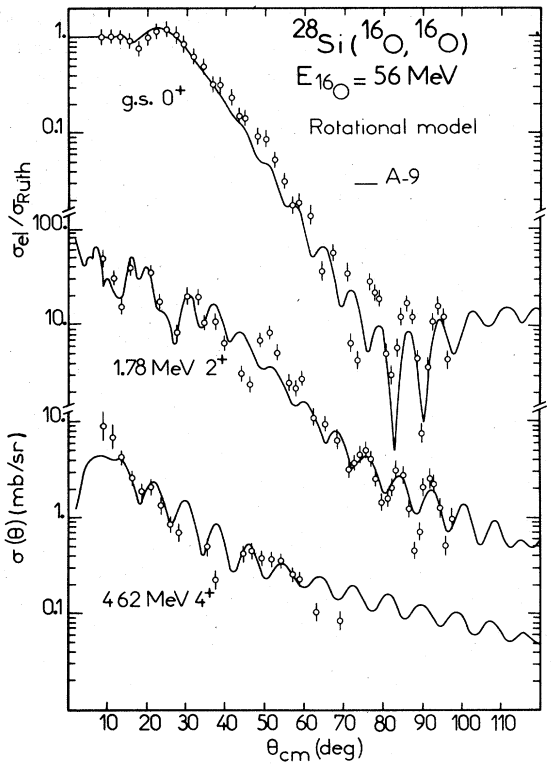

FIG. 10. Coupled-channel analysis for the elastic and 2_1^+ and 4_1^+ inelastic scattering of 56 MeV ^{16}O from ^{28}Si with the potential A-9. The 0_g^+-2_1^+-4_1^+ ground state rotational coupling scheme is chosen.

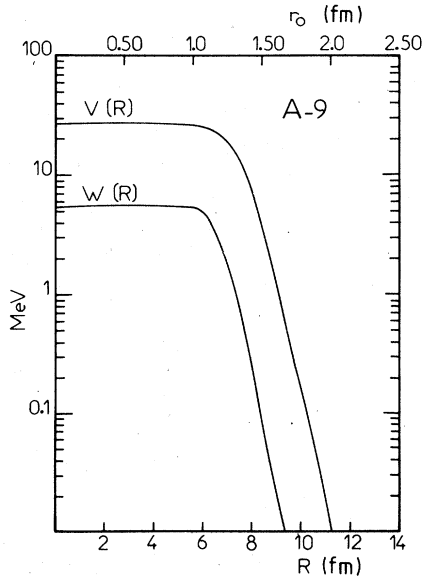

FIG. 11. Real and imaginary part of the potential A-9.

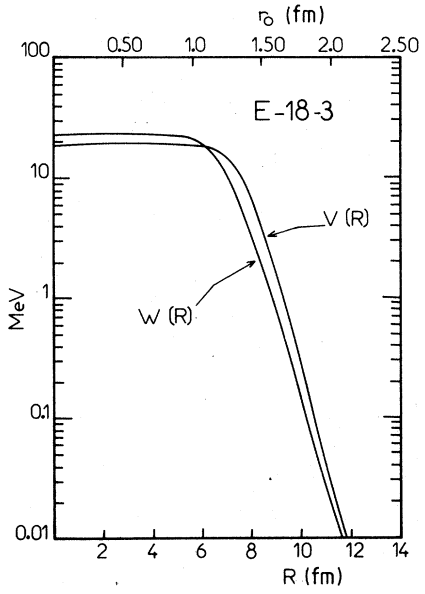

FIG. 12. Real and imaginary part of the potential E-18-3.

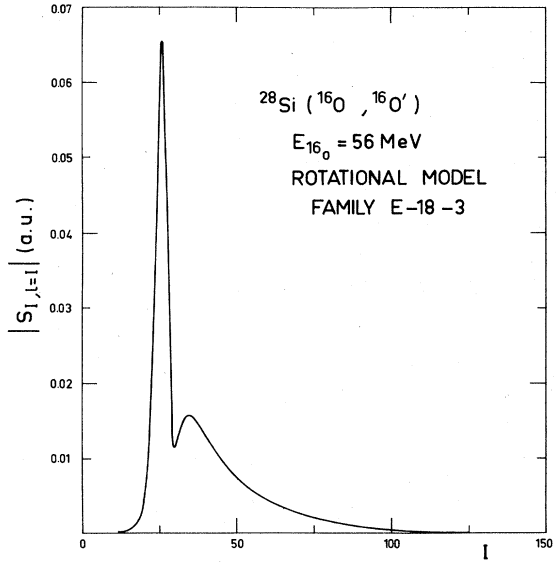

FIG. 13. Absolute magnitudes of the transition matrix elements for the 2_1^+ inelastic scattering as a function of the total channel spin I for the partial waves $l=I$, calculated with the E-18-3 potential.

potentials. As can be seen in Fig. 13, the curve of E-18-3 has a normal behavior: The first peak near the grazing partial wave is due to nuclear excitation and the second broad one is originated from Coulomb excitation. We can expect a strong destructive interference between Coulomb and nuclear excitation since their form factors are of opposite sign. However, in Fig. 14 the S matrix corresponding to family A-9 presents a very different behavior: There is a satellite peak for a partial wave $l = 20$, smaller than the grazing partial wave ($l_g = 24$). It is probable that this structure is responsible for the calculated wiggles at backward angles in the 2^+ inelastic angular distribution.

The four-parameter optical model potentials with an equal geometry have also been attempted both for the $0_g^+ - 2_1^+$ coupling and the $0_g^+ - 2_1^+ - 4_1^+$ coupling, and provide also similar fits to ones obtained with A-3 and A-9, respectively. We just list these potentials respectively as S-5 and S-6 in Table II. It can be noticed that these potentials are very similar to S-1 but less absorptive as expected.

It was again found from the coupled-channel calculations that the 0_g^+ and 2_1^+ angular distributions measured[2] up to 180° at 55 MeV cannot be reproduced by an equal geometry potential but only by a six-parameter potential. In Fig. 15 we display the results obtained with the six-parameter potential S-23. It is very difficult to reproduce the backward angle behavior, especially for the 2_1^+ state. The S-23 has the same characteristics as S-20 corresponding to the optical model analysis: the effective potential showing pockets in the grazing wave region, a large surface transparency, and a sharp imaginary diffusivity. The transition matrix element between the 0_g^+ and 2_1^+ state is also presented in Fig. 16 and exhibits the same behavior as the one corresponding to the 56 MeV scattering data, shown in Fig. 14.

We have thus learned from this coupled-channel analysis that conclusions drawn in the optical model analysis are still valid and coupled-channel effects do not play a vital role in explaining the backward angle rise appeared in the $^{28}Si + ^{16}O$ scattering.

We have also performed a coupled-channel calculation assuming a prolate deformation of $^{28}Si(\beta_2 > 0)$. The results show that the quality of the fit for the 2_1^+ state becomes worse at backward angles; the calculated cross sections are smaller by a factor of 20. It seems possible to discriminate between prolate and oblate shape in this manner. It would be very interesting to investigate this point with further experiments and analysis on different nuclei. The corresponding optical potential S-24 is listed in Table II. Also we found

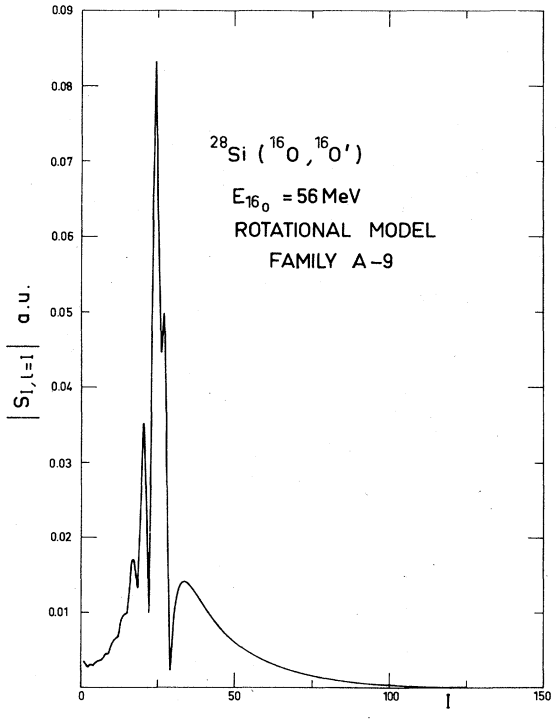

FIG. 14. Same as Fig. 13, but obtained with the A-9 potential.

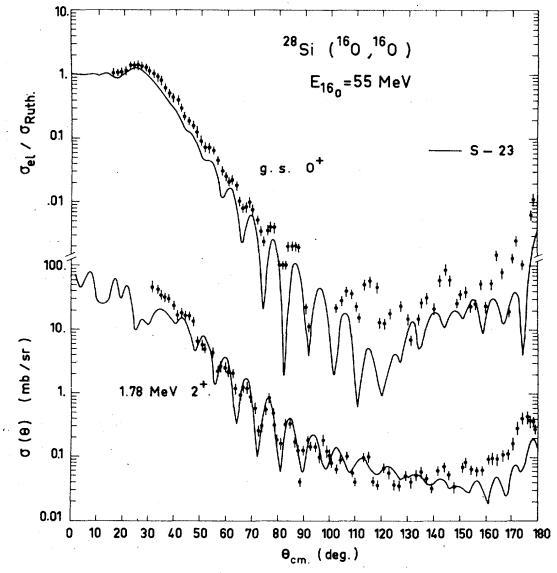

FIG. 15. Coupled-channel analysis for the elastic and 2_1^+ inelastic scattering of 55 MeV ^{16}O form ^{28}Si with the potential S-23. The rotational coupling between the 0_g^+ and 2_1^+ states is considered. The data were again taken from Ref. 2.

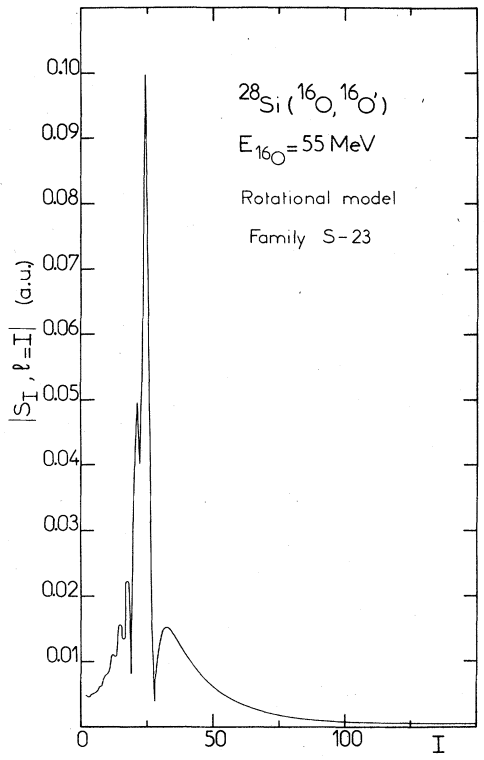

FIG. 16. Same as Fig. 13, but obtained with the potential *S*-23.

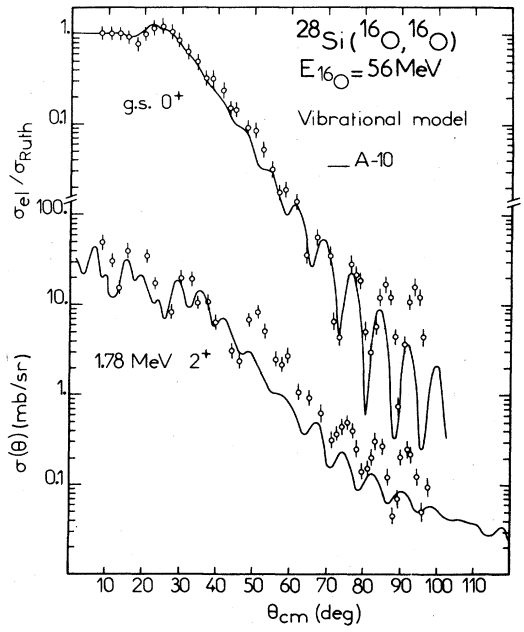

FIG. 17. Elastic and inelastic angular distributions calculated with the vibrational coupling model. All the low-lying collective states up to the 6.88 MeV 3^- level in ^{28}Si are coupled together. The optical model parameter set *A*-10 is used.

that the reorientation matrix elements taken into account in this analysis play an important role. If they are turned off, the amplitude of the oscillations in the 2_1^+ angular distribution decreases dramatically and no more reasonable fits can be obtained.

An attempt has been made in order to couple all low-lying excited levels of ^{28}Si up to the 6.88 MeV 3^- state on the basis of a vibrational model following Tamura[16]: The 1.78 MeV 2^+ state is treated as a one-phonon state, the 4.62 MeV 4^+ and 4.98 MeV 0^+ states as pure harmonic two-quadrupole phonon states. Only two deformation parameters, β_2 and β_3, were used in the calculation. An automatic search on all the optical model and deformation parameters was done. The re-

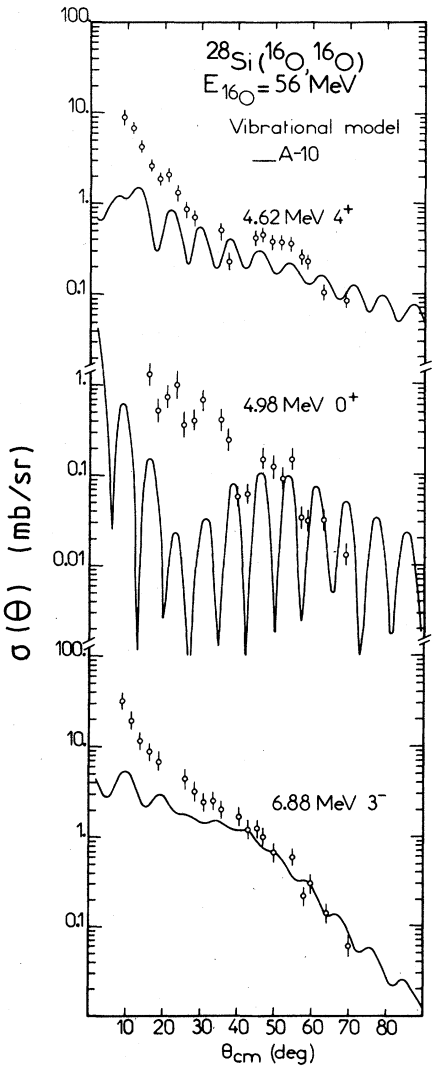

FIG. 18. Coupled-channel fits to the 4.62 MeV 4_1^+, 4.98 MeV 0_2^+ and 6.88 MeV 3^- states. Fits are obtained from the same calculation as of Fig. 17.

sulting best fits are presented in Figs. 17 and 18. The main defect concerns the absence of strong enough oscillations at backward angles in the calculated elastic and 2_1^+ inelastic angular distributions. The fit to the 4.98 MeV 0^+ state is also very poor, the calculated cross section has a too strong oscillatory behavior. The reaction mechanism is not well described by such a simple parametrization using only two constants of coupling: β_2 and β_3. The neglect of any reorientation effects due to the static quadrupole moment of the excited states could be another reason for the poor fits.

We now turn to discuss the deformation parameters, β_λ, extracted from the present coupled-channel analysis and listed in Table III. There is a well known ambiguity between absorption and deformation parameters, namely between W and β_λ.[16] The invariant quantity in the coupled-channel formalism is in fact the deformation length $\beta_\lambda R_T$ rather than β_λ itself, where R_T is the target radius. This deformation length is close, only in the case of the strong absorptive potentials, to the ones deduced from light-ion experiments, Coulomb excitations or lifetime measurements. Otherwise in the case of the weak surface absorption, the value βR_T is too small by 30%, but still comparable to the results from other heavy-ion inelastic scattering analysis.[17] For the 55 MeV data, it has to be noticed that $\beta_2 R_T$ is 1.3 which is a fairly large value, nevertheless the 2_1^+ calculated cross sections at backward angles is still small (see Fig. 15).

In Fig. 19 are finally presented the elastic and first 2^+ inelastic cross sections of the ^{18}O on ^{28}Si at 56 MeV incident energy. Almost no-oscillation appears at the backward angles in contrast with the ^{16}O measurements. The calculated angular distributions correspond to the E-18-3 family (strong absorption) with the same β_2 value as in the case of ^{16}O inelastic scattering. It can be concluded that there is no need for surface transparency in the case of ^{18}O scattering on ^{28}Si, due

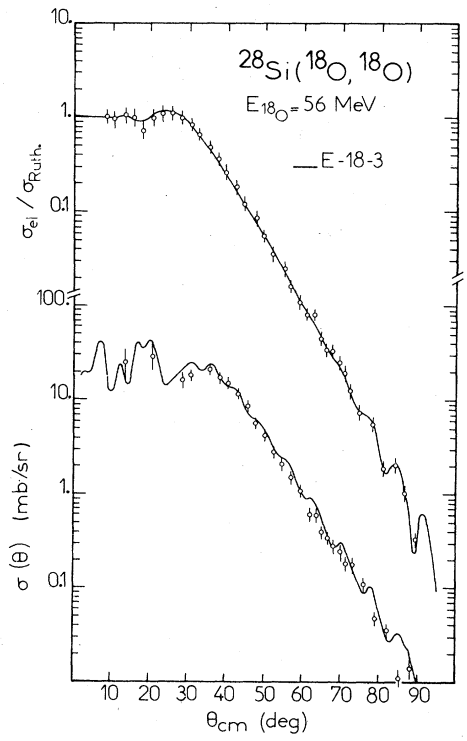

FIG. 19. Coupled-channel analysis for the elastic and 2_1^+ inelastic scattering of 56 MeV ^{18}O from ^{28}Si, with the potential E-18-3.

TABLE III. Deformation parameters obtained from coupled-channel analysis. The coupled-channel analyses have been performed on the elastic and inelastic angular distribution of the $^{28}Si(^{16}O, ^{16}O)$ reactions measured at 56 and 55 MeV incident energy.

OM set	Coupled model	$\beta_2^N=\beta_2^C$	$\beta_2 R_T$ [d] (fm)	Energy (MeV)
E-18-3	Rotational	−0.342	−1.436	56.0
A-3	Rotational	−0.274	−1.126	56.0
A-9	Rotational	−0.274	−1.126	56.0
A-10 [a]	Vibrational	0.221	1.159	56.0
S-5	Rotational	−0.223	−0.850	56.0
S-6	Rotational	−0.274	−1.040	56.0
S-23	Rotational	−0.338	−2.296	55.0
S-24	Rotational	+0.447	+1.713	55.0
Experiment [b]			−1.603	
Adopted value [c]			−1.507	

[a] $\beta_3^N=\beta_3^C=0.197$, $\beta_3 R_T=0.816$.
[b] Mermaz *et al.*, Phys. Rev. 187, 1466 (1969).
[c] Endt and van der Leun, Nucl. Phys. A214, 199 (1973).
[d] The target radius R_T is chosen as $R_T=r_v A_T^{1/3}$.

to the following reasons: First of all, more inelastic channels are open in the case of ^{18}O than in the case of ^{16}O, since ^{18}O has several collective low-lying excited states. Second, many direct transfer reactions are well Q matched either for the ground state or for the higher excited states. A comparison of the Q matching between the various direct transfer channels for ^{16}O and ^{18}O projectile is made in Table IV. The optimum Q value is given, in the vicinity of the Coulomb barrier by the most simple formula,

$$Q_{\text{opt}} = \left(\frac{Z_f z_f}{Z_i z_i} - 1\right) E_{\text{c.m.}}$$

with the usual notations. Obviously the ^{18}O projectile has more well Q matched channels than ^{16}O.

V. SUMMARY

The elastic and inelastic scattering of ^{16}O and ^{18}O on ^{28}Si at 56 MeV incident ion energy were measured up to 100° (c.m.). The data were analyzed in terms of the optical model and coupled-channel theories. The analysis was extended to the 55 MeV ^{16}O scattering on ^{28}Si measured up to 180° by the Stony Brook-Brookhaven group.

The backward angle studies of the elastic and inelastic scattering in the vicinity of the Coulomb barrier yield information on the nature of the optical model potential. There is an interplay between diffractive and refractive phenomena in the case of a system of magic nuclei such as ^{16}O and ^{28}Si. Orbiting phenomena seem to be present and a potential deep enough to exhibit pockets in the effective potentials near the grazing wave is necessary to reproduce the backward angle angular distributions. Furthermore the absorption has to be weak enough in the surface in order that the scattered particle can feel these pockets. A reflective phenomena due to a very sharp imaginary potential helps also to reproduce the data.

The nucleus ^{28}Si is better described by a rotational model than by a vibrational model. Furthermore an oblate deformation has to be assumed in the coupled-channel calculations. The deformation parameters extracted from this analysis are too small by 30% compared with Coulomb excitation and light-ion experiments, and this seems to be due to the large surface transparency, which has to be used in order to account for the backward angle scattering.

TABLE IV. Reaction Q values. g.s.–g.s. reaction Q value compared to optimum Q value for reactions induced by ^{16}O and ^{18}O ions on ^{28}Si target.

OUT \ IN	^{18}O (MeV)	^{16}O (MeV)	Q_{opt} (MeV)
^{10}C	−7.31	−12.00	
^{11}C	−4.07	−10.29	
^{12}C	−7.65	−0.21	−5.0
^{13}C	1.19	−10.36	
^{14}C	0.72	−15.18	
^{13}N	−1.28	−7.13	
^{14}N	−0.83	−8.89	−2.2
^{15}N	2.06	−9.38	
^{16}N	−7.75	−24.76	
^{14}O	−6.19	−9.80	
^{15}O	−2.18	−7.19	
^{16}O	6.89	0.00	0.0
^{17}O	0.43	−13.03	
^{18}O	0.00	−18.30	
^{17}F	−6.01	−10.98	
^{18}F	−6.29	−14.89	1.6
^{19}F	−3.59	−15.83	
^{20}Ne	0.98	−5.25	
^{21}Ne	−3.35	−15.02	2.5
^{22}Ne	−0.32	−17.82	

It is a pleasure to thank Dr. J. Raynal for his assistance with the code ECIS-73 and Dr. P. Braun-Munzinger for making his 55 MeV ^{16}O scattering on ^{28}Si data available to us.

[1]J. G. Cramer, R. M. DeVries, D. A. Goldberg, M. S. Zisman, and C. F. Maguire, Phys. Rev. C 14, 2158 (1976).
[2]P. Braun-Munzinger, G. M. Berkowitz, T. M. Cormier, C. M. Jachcinski, J. W. Harris, J. M. Barrette, and M. J. Levine, Phys. Rev. Lett. 38, 944 (1977).
[3]R. M. DeVries, D. A. Goldberg, J. W. Watson, M. S. Zisman, and J. G. Cramer, Phys. Rev. Lett. 39, 450 (1977).
[4]J. Raynal, Saclay Report No. DPh-T 69/42 (unpublished); and private communication.
[5]J. B. Marion and F. C. Young, *Nuclear Reaction Analysis* (North-Holland, Amsterdam, 1968); D. J. Weber, N. M. Hintz and D. Dehnhard, Nucl. Instrum. Methods 124, 317 (1975).
[6]V. Shkolnik, D. Dehnhard, S. Kubono, M. N. Franey, and S. Tripp, Phys. Lett. 74B, 195 (1978).
[7]A. J. Baltz and S. Kahana, Phys. Rev. C 17, 555 (1978).
[8]E. H. Auerbach, A. J. Baltz, M. Golin, and S. Kahana, in Proceedings of the Symposium on Heavy-Ion Elastic Scattering Rochester, New York, 1977 (unpublished).
[9]W. H. Miller, J. Chem. Phys. 51, 3631 (1969).
[10]S. Kubono, P. D. Bond, and C. E. Thorn, report (unpublished).
[11]T. Udagawa, in *Proceedings of the International Conference on Nuclear Structure, Tokyo, Japan, 1977,* edited by T. Marumori (Physical Society of Japan, Tokyo, 1978).
[12]P. M. Endt and C. van der Leun, Nucl. Phys. A214, 199 (1973).

[13]K. Nakai, J. L. Quebert, F. S. Stephens, and R. M. Diamond, Phys. Rev. Lett. 24, 903 (1970).
[14]O. Hausser, B. W. Hooten, D. Pelte, T. K. Alexander, and H. C. Evans, Phys. Rev. Lett. 23, 320 (1969).
[15]R. de Swiniarski, F. G. Resmini, D. L. Hendrie, and A. D. Bacher, Nucl. Phys. A261, 111 (1976).
[16]T. Tamura, Rev. Mod. Phys. 32, 679 (1965).
[17]D. S. Gale and J. S. Eck, Phys. Rev. C 7, 1950 (1973).